

Available online at www.sciencedirect.com

jmr&t
Journal of Materials Research and Technology
journal homepage: www.elsevier.com/locate/jmrt



Processing condition dependency of increased layer thickness on surface quality during electron beam powder bed fusion

Yufan Zhao ^{a,b}, Kenta Aoyagi ^{c,*}, Kenta Yamanaka ^c, Akihiko Chiba ^c

^a State Key Laboratory of Solidification Processing, Northwestern Polytechnical University, Xi'an, Shaanxi 710072, PR China

^b Research & Development Institute of Northwestern Polytechnical University in Shenzhen, Shenzhen, Guangdong 518063, PR China

^c Institute for Materials Research, Tohoku University, 2-1-1 Katahira, Aoba-ku, Sendai, Miyagi 980-8577, Japan

ARTICLE INFO

Article history:

Received 4 July 2023

Accepted 28 August 2023

Available online 1 September 2023

Keywords:

Additive manufacturing
Electron beam melting
Powder layer thickness
Thermophysical property
Forming quality

ABSTRACT

The energy beam and powder layer interaction influences the dynamic melt behavior and determines the surface quality in electron beam powder bed fusion (PBF-EB). It is generally believed that increasing the powder layer thickness favors production efficiency but is contradictory to improving the forming quality. How variations in the powder layer thickness affect the interaction between the electron beam and the powder bed, which influences the melt behavior and resultant surface quality, has not been well understood. In this study, cylindrical specimens with increased nominal layer thicknesses from 80 to 140 μm were prepared using PBF-EB. The study verified the processing feasibility of ensuring the forming quality under a high layer thickness. Within the processing regime of this study, a relatively large powder layer thickness expanded the processing window. According to the thermophysical-property analysis of the powder bed, the emissivity and thermal conductivity exhibited upward and downward trends, respectively, with increased powder layer thickness. The increased thickness reduced the fusion efficiency, restricting the height difference within the overall sample surface caused by overheating. The numerical simulation clarified the dependence of the layer thickness-effect on the processing conditions. The proportion of incomplete melted powder in the electron beam irradiating area increased at a high scan speed. Subsequently, the hindering effect on heat absorption and transfer caused by the powder layer and its increased thickness was fully manifested. That is, the evolution trend of melt behavior and surface morphology resulting from increased layer thickness is remarkable at high scan speeds.

© 2023 The Author(s). Published by Elsevier B.V. This is an open access article under the CC BY-NC-ND license (<http://creativecommons.org/licenses/by-nc-nd/4.0/>).

1. Introduction

The excellent forming quality and target properties of additively manufactured parts depend on accurately controlling the process parameters. Metal powder melting is one of the

primary forming methods for metal additive manufacturing (AM) in high-end equipment manufacturing fields, such as aerospace, automobiles, and energy [1]. Consequently, the processing parameters related to the powder and its transportation can significantly impact the forming quality [2]. In the powder bed fusion (PBF) process, the layer thickness,

* Corresponding author.

E-mail address: kenta.aoyagi.e7@tohoku.ac.jp (K. Aoyagi).

<https://doi.org/10.1016/j.jmrt.2023.08.288>

2238-7854/© 2023 The Author(s). Published by Elsevier B.V. This is an open access article under the CC BY-NC-ND license (<http://creativecommons.org/licenses/by-nc-nd/4.0/>).

packing density, and uniformity of the powder layer directly influence the interaction between the high-energy beam (laser [3] or electron beam [4]) and the powder layer, as well as the corresponding dynamic melt behavior [5], thus determining the internal defect forming tendencies and the surface quality of the fusion layer [6].

Electron beam powder bed fusion (PBF-EB) is an AM technique based on exposing a metal powder to an electron beam and melting it [7]. Although the essential function and selective melting process of the metal powder layer are common to laser PBF, the electron beam deflection relies on electromagnetic control without mass and inertia rather than the mechanical mirror that is applicable to laser techniques; thus, the electron beam can be located almost instantaneously over the entire building area, and simultaneously handle multiple molten pools [8]. Moreover, an electron beam exhibits deeper penetration into powder layers than a laser beam and can theoretically be assumed to possess a relatively high forming efficiency with an ability to melt an extensive range of powder layer thicknesses [9]. It is generally believed that increasing the powder layer thickness does not improve the forming quality during the PBF process [10]. Consequently, in conventional experiments and production, the applied layer thickness is close to the mean powder particle size, based on empirical engineering practices [11]. This is to ensure sufficient powder to be laid and coated during the initial stage of forming without impairing the forming quality. For PBF-EB, the feasibility of increased layer thickness for processing has attracted the researchers' attention.

To date, research on the effect of layer thickness on forming quality has focused primarily on laser PBF (PBF-L). The effect of increasing the powder layer thickness on densification [12] and surface finish [13] has been studied. Other studies have suggested that a high layer thickness improves productivity [14]. However, the extensively increased layer thickness reduces density and accuracy and increases surface roughness, resulting from the more easily formed melt agglomerate and lack of fusion [15]. With increasing layer thickness, multiple laser reflections between particles can be promoted to some extent, which could enhance laser energy absorption [16]. However, excessive layer thickness weakens the wetting effect between the melt and the substrate plane, which easily coalesces and agglomerates under the action of surface tension [17]. Inhomogeneous melting with a rugged melt-track profile can lead to internal porosity and increased surface roughness [18]. Notably, owing to the different physical characteristics of the laser and electron beam [19], the influence mechanism of powder layer thickness variations on the interaction between the powder and electron beam must differ. Regarding energy absorption, PBF-L is affected mainly by the surface morphology of the powder bed [20], while PBF-EB is dominated by its thermophysical properties [21]. Only a few studies have been performed to evaluate the feasibility and effect of a high layer thickness on PBF-EB-built parts. A representative study conducted by Li et al. [22] showed that even if the powder layer thickness increased to 300 μm , dense samples (density $\geq 99.5\%$) could be obtained. Although the high layer thickness inherently increases the surface roughness owing to the more pronounced stochastic effect of the

powder layer, applying an augmented accelerating voltage (90 kV) can improve the surface finish by increasing the melt penetrability [9]. It is evident that compared with PBF-L, PBF-EB is less sensitive to the powder layer thickness. Nevertheless, how variations in the powder layer thickness affect the interaction between the powder bed and electron beam, as well as the influence mechanism on the melt behavior and resultant surface roughness, have not been well understood. Moreover, the processing window corresponding to the different layer thicknesses requires further investigation.

This study prepared four batches of cylindrical specimens—with increasing layer thicknesses from 80 to 140 μm —using PBF-EB within the same range of processing parameters. The sample surface roughness was characterized and classified to derive the processing windows using different powder layer thicknesses. Changes in the surface roughness with the layer thickness were analyzed. Combined with thermophysical-property analysis of the powder bed and numerical simulation of the heat and mass transfer, the influence mechanism of the layer thickness on the melt behavior and resultant surface quality was determined, and the dependence of the layer thickness-effect on the processing conditions was clarified. This research lays a scientific foundation for successfully implementing efficient PBF-EB building by applying appropriate powder layer thicknesses and matching processing conditions.

2. Materials and methods

2.1. Materials and PBF-EB process

Ti6Al4V alloy powders fabricated using the plasma rotating electrode process (JAMPT Corporation, Miyagi, Japan) were used for PBF-EB building trials. The scanning electron microscopy (SEM) results in Fig. 1(a) show particles with excellent sphericity, which can contribute to a smooth powder flow. The particle size distribution (PSD) was measured using a laser diffraction particle size analyzer (MT3200, Microtrac Retsch GmbH, PA, US).

As shown in Fig. 1(b), the PSD has a Gaussian distribution with a mean diameter of 85.18 μm . Four batches of cylindrical samples were built with nominal layer thicknesses of 80, 100, 120, and 140 μm . For each batch of forming experiments, 29 samples were dislocated on a SUS304 substrate, as shown in Fig. 1(c). Fig. 1(d) shows the diameter and height of the cylindrical sample to be 20 mm, with a 3-mm high support structure being set between the sample bottom and the substrate. PBF-EB building trials were conducted using an Arcam EBM Q20plus system (GE Additive, West Chester, OH, US). A bidirectional scanning mode with 90° rotation between layers was applied to the built sample. The processing parameters of each sample are listed in Table 1. The beam diameter determined by focus offset was about 300 μm . The electron beam power (P) is equal to the product of the current and acceleration voltages. This study used the speed function [23], so the calculated scan speed (V) is also listed. The beam current used for preheating the powder layer was 43–48 mA, and during the building process, the pressure in the vacuum chamber was 10^{-2} mbar.

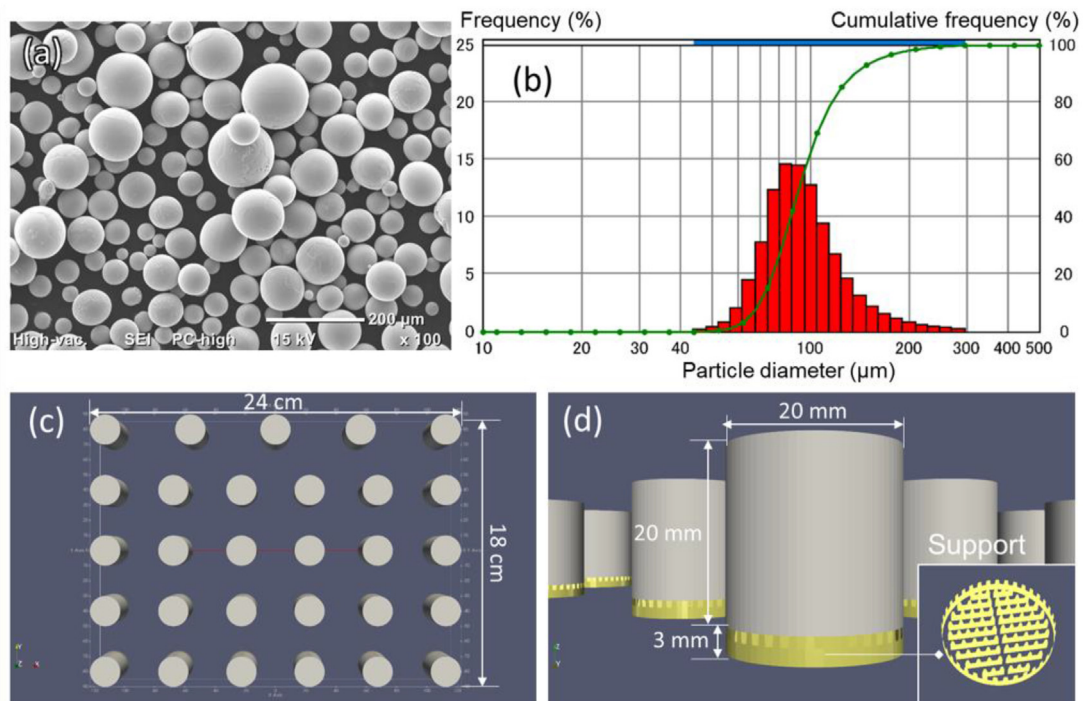


Fig. 1 – (a) Scanning electron microscopy image of the Ti6Al4V powder particles with (b) a Gaussian distribution of the particle size. (c) For each batch of forming experiment, 29 samples are dislocated on a SUS304 substrate. (d) The cylindrical samples have a diameter and height of 20 mm, with a 3-mm high support structure being set between the sample bottom and the substrate.

Table 1 – The PBF-EB processing parameters for each sample.

No.	Voltage (kV)	Current (mA)	Power (W)	Speed function	Calculated scan speed (mm/s)	Line offset (mm)	Focus offset (mA)
1	60	5	300	25	157.4833	0.18	35
2		5	300	20	128.025	0.18	
3		8	480	20	246.6667	0.18	
4		10	600	20	412.3611	0.18	
5		5	300	25	157.4833	0.18	
6		8	480	25	305	0.18	
7		10	600	25	510.2778	0.18	
8		5	300	30	186.9417	0.18	
9		8	480	30	363.3333	0.18	
10		10	600	30	608.1944	0.18	
11		5	300	25	157.4833	0.2	
12		5	300	20	128.025	0.2	
13		8	480	20	246.6667	0.2	
14		10	600	20	412.3611	0.2	
15		5	300	25	157.4833	0.2	
16		8	480	25	305	0.2	
17		10	600	25	510.2778	0.2	
18		5	300	30	186.9417	0.2	
19		8	480	30	363.3333	0.2	
20		10	600	30	608.1944	0.2	
21		5	300	20	128.025	0.22	
22		8	480	20	246.6667	0.22	
23		10	600	20	412.3611	0.22	
24		5	300	25	157.4833	0.22	
25		8	480	25	305	0.22	
26		10	600	25	510.2778	0.22	
27		5	300	30	186.9417	0.22	
28		8	480	30	363.3333	0.22	
29		10	600	30	608.1944	0.22	

2.2. Characterization

The upper surface roughness of each sample was measured using a 3D measurement system with a wide-area (Keyence VR-3200, Keyence Corporation, IL, US) to evaluate the surface quality. The measurement indexes S_a (arithmetical mean height) and S_{dr} (developed interfacial area ratio) of the surface roughness were characterized to evaluate the surface quality with different measurement standards. S_a denotes the absolute value of the height difference at each point compared with the arithmetic mean value of the surface [24]—that is, S_{dr} is the additional surface area percentage caused by the surface texture compared with the surface projection area [25]. Consequently, S_a denotes the ups and downs of the surface, whereas S_{dr} reflects greater stress on the surface texture. Additionally, the sample density was measured using the Archimedes drainage method.

2.3. Numerical simulation

To determine how variations in the powder layer thickness affect the interaction between the powder bed and electron beam, as well as the influence mechanism on the melt behavior and the resultant surface roughness, a numerical framework was developed for powder bed generation and single-track fusion using an electron beam. The simulation data of the powder bed with different nominal layer thicknesses were obtained using YADE [26] software based on the discrete element method (DEM) [27]. Under the control of the contact law [28], the geometric data of particle arrangement in the powder bed were obtained using powder-spread simulations with inputs of PSD, density, elastic modulus, and other Ti6Al4V powder characteristic parameters (Table 2). The specific model and related settings can be found in previous studies [21].

Then the single-track melting simulation was performed. The powder bed data (as the computational domain) were then imported into the computational thermo-fluid dynamic (CtFD) [29] simulation implemented using the Flow 3D multiphysics-modeling software [30] coupled with an AM module. Because the PBF-EB processing chamber is maintained in a vacuum, the cooling effect caused by gas convection can be ignored [31]; thus, the heat transfer in the computational domain primarily involves heat conduction and radiation. The circular electron beam volumetric heat

Table 2 – Parameters and particle properties applied in the DEM simulation.

Input parameters	Values
Particle density	4420 kg/m ³
Young's modulus of particle	110 GPa
Young's modulus of substrate	193 GPa
Poisson's ratio of particle	0.342
Poisson's ratio of substrate	0.250
Dynamic friction coefficient of interparticle	0.531
Dynamic friction coefficient between particles and base plate	0.239
Interparticle restitution coefficient	0.15
Restitution coefficient between particles and base plate	0.30

source with a Gaussian energy distribution has a certain penetration depth. The energy distribution in the depth direction was modeled in a previous study [32]. Moreover, the energy utilization rate was set to 90% [33]. The thermophysical properties of the Ti6Al4V alloy applied in the CtFD simulations are shown in Table 3. The boundary conditions of the computational domain can be referred to in the study [34]. Other numerical applications of parameters/coefficients and model validation can be found in previous studies [35]. The initial temperature of the computational domain was set at 700 °C, the default preheating temperature for Ti6Al4V alloy in Arcam EBM Q20plus system.

3. Results

3.1. Processing window

At first, Archimedes' method was applied to determine the specific densities of all samples. Except for the samples that failed to form, the specific density of all other samples is greater than 98.5%. Overall, dense samples were obtained; thus, this work focused on the forming quality of the upper surface. This study determined the processing window for different nominal layer thicknesses based on the surface quality of PBF-EB built samples. Notably, the overall height fluctuation/difference and surface texture/stripes must be measured by distinct indicators. Although the sample shown in Fig. 2(a) has a smoother surface than that shown in Fig. 2(b), it has a relatively higher S_a value because of its higher bulge height at the edge—in other words, it may be not easy to evaluate surface quality objectively and comprehensively using only S_a . With the introduction of S_{dr} , the rough texture of the sample shown in Fig. 2(b) can be truly reflected. Based on the above considerations, this study classified the surface quality by setting thresholds for both S_a and S_{dr} before deriving the processing window. When $S_a \leq 45 \mu\text{m}$ and $S_{dr} \leq 0.05$, the surface profile can be defined as Smooth and Even (Fig. 2(c)); when $S_a \leq 80 \mu\text{m}$ and $S_{dr} > 0.05$, it can be defined as Even

Table 3 – Parameters and Ti6Al4V properties applied in the CtFD simulation.

Input parameters	Symbol and unit	Value
Density	ρ (g/cm ³)	3.75 ~ 4.42
Viscosity	μ (mPa·s)	2.36 ~ 3.25
Thermal conductivity	κ (W/m·K)	7.00 ~ 34.6
Specific heat	C_p (J/kg·K)	546 ~ 831
Emissivity	ϵ	0.224
Liquidus temperature	T_L (K)	1923
Solidus temperature	T_S (K)	1873
Boiling point at standard atmospheric pressure	T_{V1} (K)	3533
Latent heat of fusion	ΔH_{SL} (J/kg)	2.86e+05
Latent heat of vaporization	ΔH_{LV} (J/kg)	9.83e+06
Surface tension at T_L	γ_L (J/m ²)	1.525
Temperature coefficient of surface tension	$\frac{d\gamma}{dT}$ (J/m ² ·K)	-0.00028
Adiabatic index	k	1.66
Stefan–Boltzmann constant	σ (W/m ² ·K ⁴)	5.67e-08
Universal gas constant	R (J/K·mol)	8.314
Initial environment temperature	T_0 (K)	298

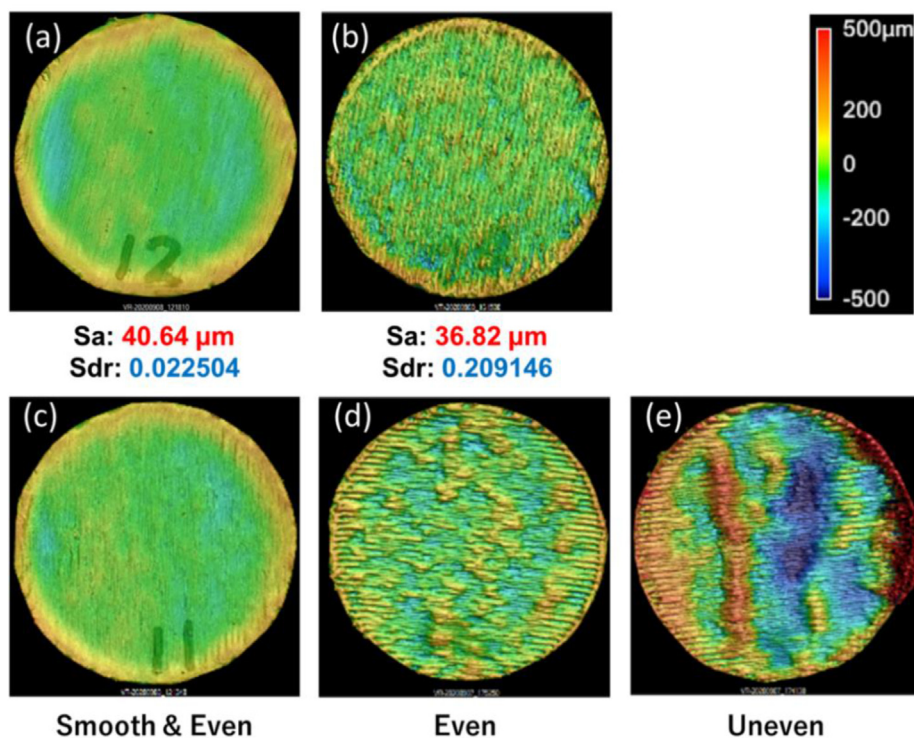


Fig. 2 – Images showing the upper surface profile. Although the sample in (a) has a smoother surface than that in (b), it has a relatively higher S_a value due to its higher bulge height only at the edge. With S_{dr} , the rough texture (relatively high S_{dr} value) of the sample can be truly reflected. The samples can be classified as (c) *Smooth and Even*, (d) *Even*, and (e) *Uneven* based on the thresholds for both S_a and S_{dr} .

(Fig. 2(d)); and when $S_a > 80 \mu\text{m}$, it can be defined as *Uneven* (Fig. 2(e)).

Since layer thickness is variable, area energy is used to establish the process map instead of volume energy. Using the above metrics, the process map for each layer thickness was drawn based on the scan speed (V) and area energy ($P/V/\text{line offset}$). As shown in Fig. 3, apart from the forming failure under a minimum layer thickness of $80 \mu\text{m}$, the sample building could be successfully constructed under other layer thickness conditions. This is because the nominal layer thickness of $80 \mu\text{m}$ is slightly smaller than the average diameter of the powder, making it easy to form a non-uniform, thin fusion layer during the initial building stage, leading to non-uniformities being more prominent during the subsequent deposition process [36]—that is, a stable and continuous fusion layer cannot be formed. With an increase in the nominal layer thickness, it is evident that not only is the forming failure eliminated, but the number of *Uneven* samples in the cases of 120- and 140- μm layer thickness is less than that in the case of 100- μm layer thickness. Additionally, the *Even* samples are located primarily in the low scan-speed region, which is related to the instability of the melt at high scan speeds.

The study verified the processing feasibility of ensuring the forming quality under a high layer thickness. Regarding the powder and layer thickness range used in this study, the relatively large powder layer thickness expands the processing window to a certain extent. The thicker the powder layer,

the greater the packing density and specific surface area of the powder bed [37]. A high packing density is conducive to increasing the sample density. Still, for electron beam melting, an increased specific surface area of the powder layer increases the thermal emissivity, thereby reducing the heat absorption in the interaction between the powder and electron beam [21]. Consequently, the evolution of fusion behavior with layer thickness in this study will be further discussed with numerical simulations.

3.2. Evolution of forming quality

It is evident from the process maps that within the regime of this study, the processing window expands with an increase in layer thickness. Specifically, Fig. 4 shows that the related forming qualities evolve with nominal powder layer thickness variations. The corresponding box plots were drawn based on the density, S_a , and S_{dr} values of each sample in the four batches of the building experiments. The box plots reflect the overall distribution characteristics of each data group for each layer thickness. The horizontal lines represent the maximum, minimum, median, and mean values.

As shown in Fig. 4(a), the sample densities decrease with the increased nominal layer thickness. However, the relative densities of all samples are greater than 98.5%, which means that in terms of density, the high layer thickness used in this study (140 μm) does not result in a perceptible reduction in density. From the perspective of surface roughness, the mean

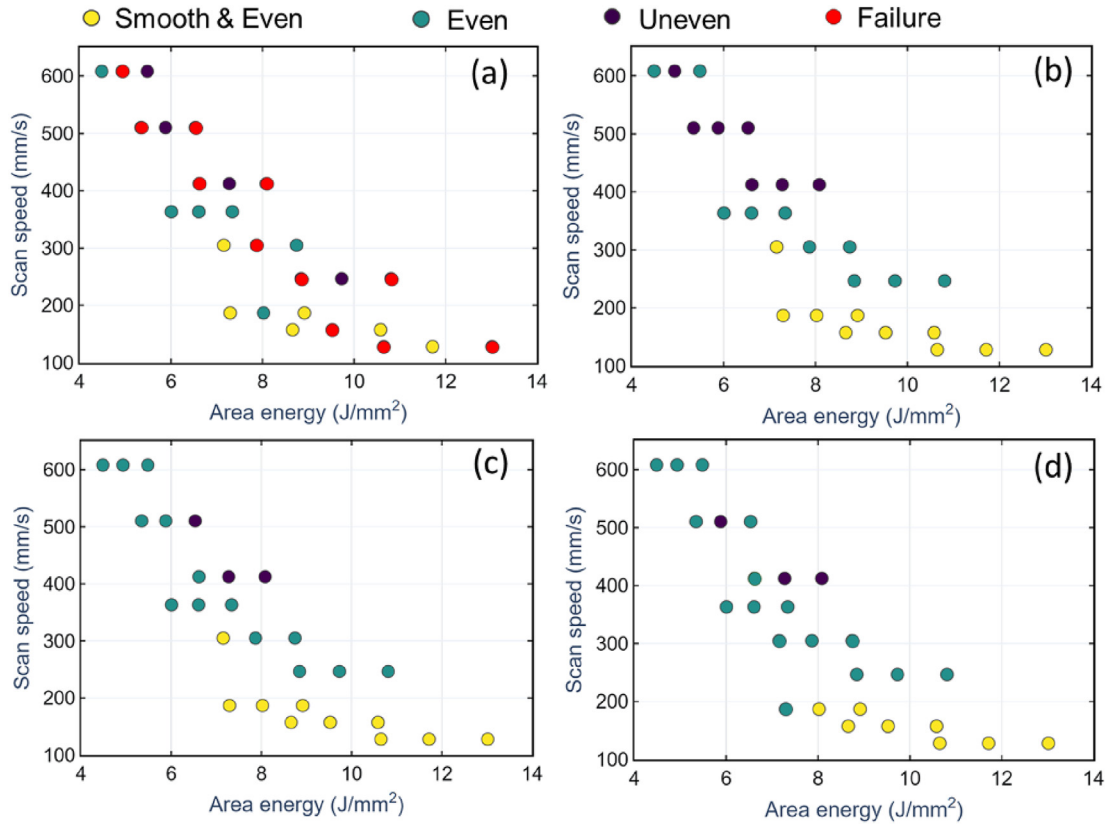


Fig. 3 – Processing map under different nominal powder layer thicknesses of (a) 80, (b) 100, (c) 120, and (d) 140 μm.

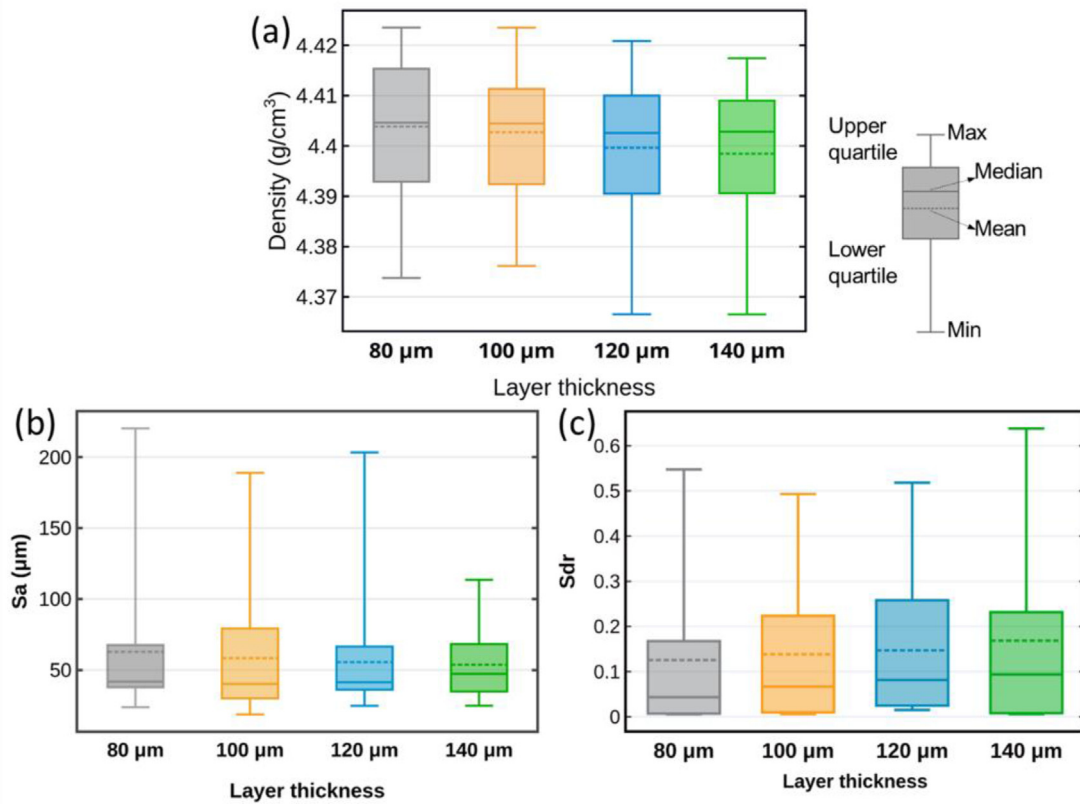


Fig. 4 – Related forming qualities in terms of (a) density, (b) S_a , and (c) S_{dr} evolve with the variations in the nominal powder layer thickness.

value of S_a decreases, and the mean value of S_{dr} increases with an increase in layer thickness—in other words, in the previous section (Fig. 3), when the layer thickness increased to more than 100 μm , the expansion of the processing window was due primarily to the decrease in S_a . When the layer thickness continued to increase to 140 μm , the increase in S_{dr} reduced the number of *Smooth and Even* samples compared to the 100- μm case. The observed relationship between the layer thickness and the dynamic melt behavior indicates that a high layer thickness helps restrain the fluctuation and reduce the height difference within the overall area of the sample's upper surface. Nevertheless, increased S_{dr} indicates that a high layer thickness contributes to forming a rough surface texture. Consequently, the effect of the powder layer thickness on the evolution of surface quality cannot be lumped under one category, while the influencing mechanism of the layer thickness needs to be further discussed from the perspective of dynamic melt behavior during the fusion process.

Consequently, examining whether the powder layer thickness is sensitive to the electron beam parameters (power and scan speed) is essential. Fig. 5 shows variations in the surface roughness S_a and S_{dr} with the power and scan speed. The results show that S_a and S_{dr} exhibit an increasing trend with increasing power and scan speed, with fluctuating values among the various conditions becoming substantial. High power tends to cause melt overheating and an oversized molten pool, while a high scan speed induces Rayleigh–Plateau instability [38].

It is worth noting that—as is evident from the dispersion of the roughness indicators S_a and S_{dr} under various processing conditions—both the overall roughness and the differences between samples are small under low power and scan-speed

conditions—that is, the effect of the powder layer thickness on the surface quality also tends to be weak. Fig. 6 shows the surface profiles of representative samples under high and low power and scan-speed conditions.

Herein, the linear energy densities of samples #27 (Fig. 6(a)) and #14 (Fig. 6(b)) are similar, but the evolution trend is inconsistent with variations in the layer thickness. Under low power and scan-speed conditions (#27: $P = 300$ W, $V = 186.94$ mm/s), the sample surface is *Even and Smooth*, and the change in surface morphology with powder layer thickness is almost imperceptible. In stark contrast, under high power and scan-speed conditions (#14: $P = 600$ W, $V = 412.36$ mm/s), the surface morphology of the samples varies from a wide range of ups and downs to small-scale bulges distributed on the surface plane with increasing layer thickness. Notably, as is evident from Fig. 6(c) and (d), with an increase in the powder layer thickness, the overall height difference of the undulation on the surface of sample #14 decreases, so the S_a value tends to decrease too, whereas an increase in the number of local bulges makes the surface texture prominent, so the S_{dr} value exhibits an upward trend. These results are consistent with the evolutionary trends shown in Fig. 4.

Whether the effect of layer thickness variation on the surface topography under a given processing condition or the sensitivity of surface quality to layer thickness under different processing conditions is actually determined by the heat and mass transfer behavior during the interaction between the powder layer and electron beam and remains to be confirmed, which would be insightful to understand the melt dynamics and mechanisms involved. In the following sections, simulation analysis explains

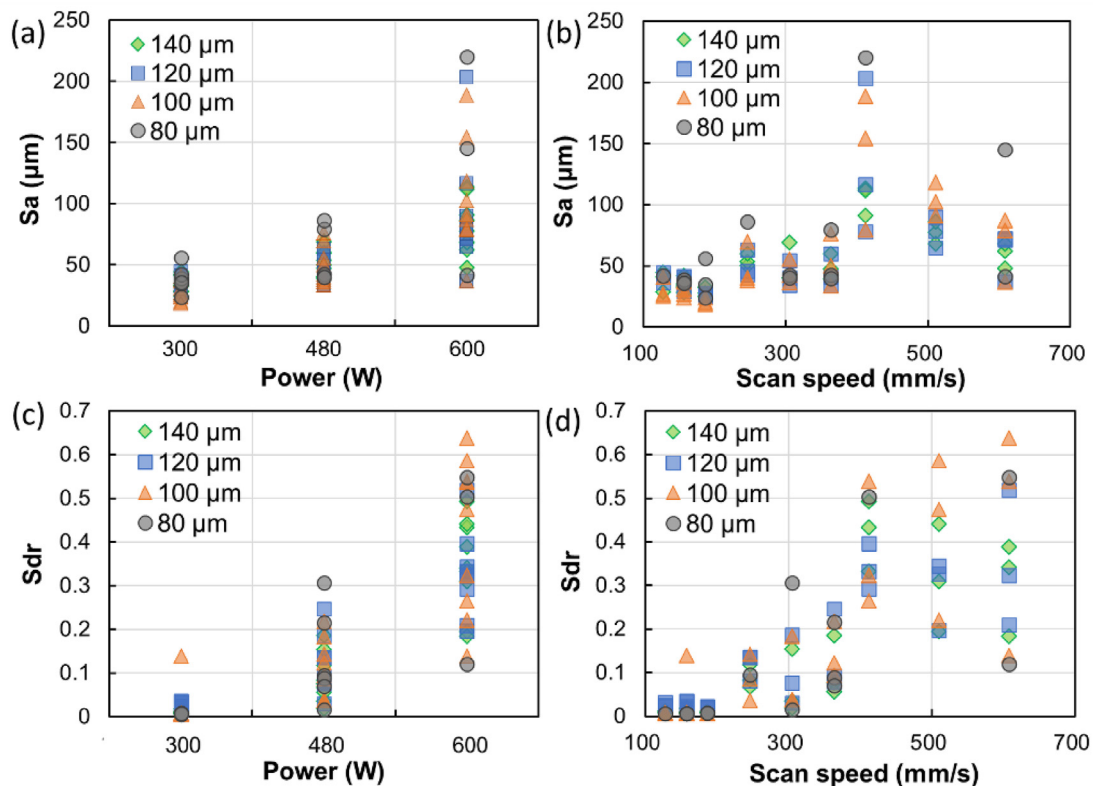


Fig. 5 – Evolution of surface roughness (a) (b) S_a and (c) (d) S_{dr} with (a) (c) power and (b) (d) scan speed.

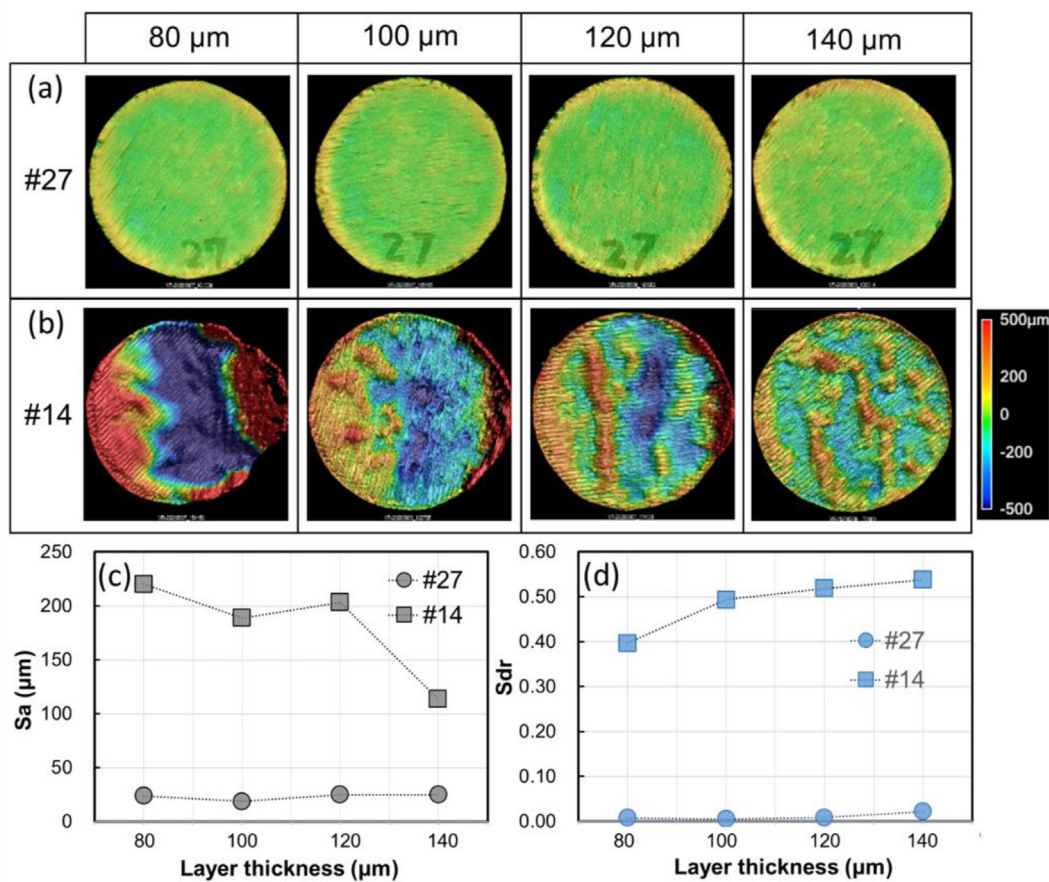


Fig. 6 – (a) (b) Surface profile of representative samples under high and low power and scan speeds conditions. Evolution of corresponding surface roughness (c) S_a and (d) S_{dr} with powder layer thickness. The linear energy density of (a) sample #27 and (b) sample #14 are close, but the evolution trend is clearly inconsistent with layer thickness variations.

the surface morphology evolution with the powder layer thickness under the above different processing conditions.

3.3. Fusion simulation illustrating melt behavior

A DEM simulation was performed considering powder bed generation to simulate the powder layer fusion process. The DEM simulations were implemented using the nominal layer thickness L_0 . As the volume of the powder layer decreases after fusion and the proportion of the solid phase is close to the original powder layer packing density, the preset layer thickness of the next layer L_n in the DEM simulation can be obtained using the equation $L_n = L_0 + L_{n-1} (1 - \rho_p)$, where ρ_p denotes the packing density of the previous layer.

After the initial several layers are deposited, the practical layer thickness reaches a stable value, as shown in Fig. 7. Herein, nominal layer thicknesses of 80 and 140 μm were selected for the simulation and comparative analysis. Inputting the geometric data of the DEM powder layer with stable layer thickness into the computational domain of the CTFD simulation, the single-track fusion simulations were then conducted under the processing conditions of samples #27 and #14 (Fig. 6).

Fig. 8 shows the melt-track profile after fusion and the melt pool geometry during the CTFD melting simulation. Under the

processing conditions of sample #27 (Fig. 8(a) and (c)), there is no obvious difference in the melt-track morphology characteristics for different layer thicknesses. The heights of the two tracks at the corresponding positions are practically consistent. The height of the melt-track front end is relatively low, which is the result of melt depression induced by Marangoni convection [39], as shown in Fig. 8(b) and (d).

By contrast, under the processing conditions of sample #14 (Fig. 8(e) and (g)), the melt-track morphology changes significantly with the powder layer thickness. The height difference between the front and rear ends of the melt track with a nominal thickness of 80 μm is large (large S_a), that is, a continuous melt track with a humping effect. Although the height difference between the front and rear ends of the melt track with a nominal thickness of 140 μm is small, the melt separation and local uplifts intensify the texture of the melt track (large S_{dr}). The characteristics of the simulated melt tracks are essentially consistent with the experimental results (Fig. 6).

As is evident from the longitudinal section of the melt pool, the effect of different layer thicknesses on the dimensions and shape of the molten pool is not significant at low power and scan speeds (sample #27). With increased power and scan speed (sample #14), the melt pool is greatly elongated, and the dimensions of the melt pool decrease with the increased powder layer thickness.

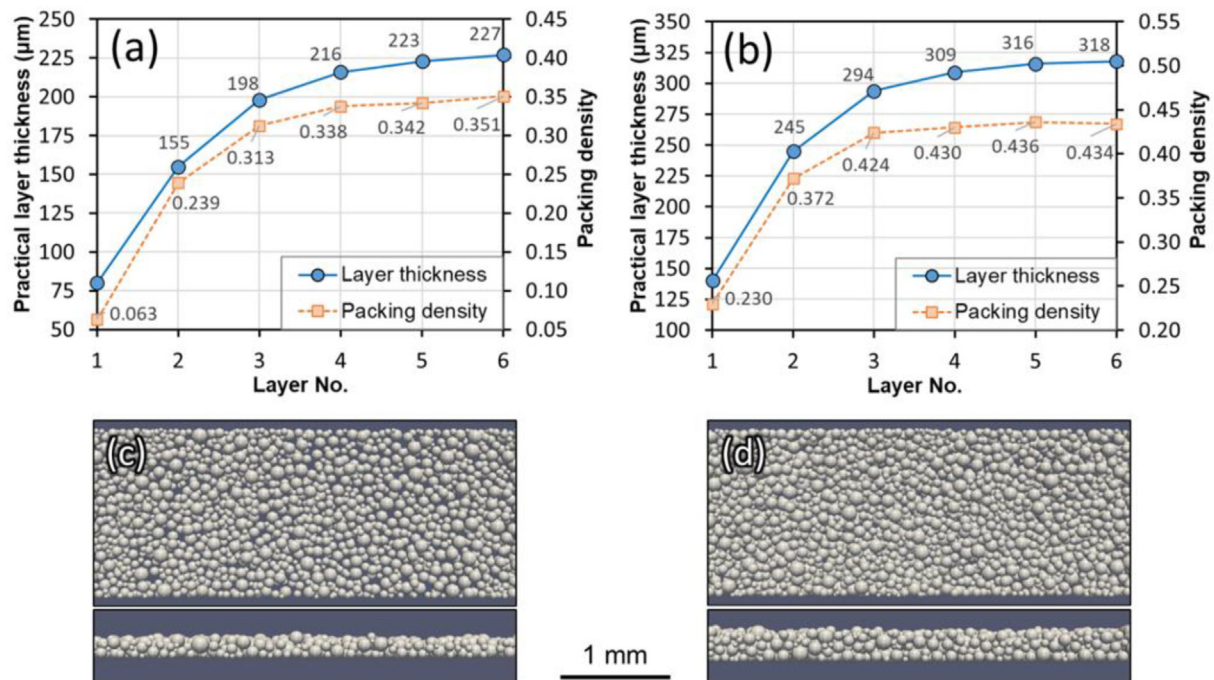


Fig. 7 – DEM simulations of powder bed generation are implemented with the nominal layer thickness of (a) (c) 80 and (b) (d) 140 μm . After depositing several initial layers, the practical layer thickness reaches a stable value. (c) (d) The geometric data of the DEM powder layer with stable layer thickness are then input into the computational domain of the CtFD simulation.

The stability of a fast-moving melt pool is closely related to its dimensional characteristics. The larger the length:width ratio of the molten pool, the more likely it is to cause Rayleigh–Plateau instability, thus promoting melt separation and spheroidization [40]. Fig. 9 shows the cross sections and corresponding dimensional data of the melt tracks under various conditions.

Herein, the fusion simulation case on a bare plate without powder is complemented for reference. Regarding the molten pool depth, differences are not apparent whether there are powder or layer thickness changes. This indicates that the penetration depth of the electron beam heat source is insensitive to surface morphology.

Next, focusing on the molten pool width evolution, compared with the bare plate, the presence of the powder layer greatly reduces the molten pool width, indicating that the powder layer limits the lateral heat transfer of the molten pool. In combination with the depth, the molten pool volume of melting on the powder bed is smaller than that on the bare plate, suggesting that the powder layer reduces the fusion efficiency and may avoid melt overheating under certain processing conditions.

Comparing the results under the processing conditions of samples #27 and #14, the molten pool width is more sensitive to variations in the powder layer thickness under high power and scan-speed conditions (sample #14). As the layer thickness increases from 80 to 140 μm , the width decreases more for sample #14 and less than that for sample #27. Considering the longer molten pool (Fig. 8), with increasing powder layer thickness, the high power and scan-speed conditions are

more prone to trigger melt separation and form local protrusions based on Rayleigh–Plateau instability. Therefore, to obtain a more stable molten pool and corresponding excellent forming quality, both power and scan speed should not be too high under a certain linear energy density.

In summary, the difference in fusion behavior caused by changes in the powder layer thickness is mainly manifested under high power and scan-speed conditions. In the following section, the mechanism of the above phenomena is discussed by combining the thermophysical properties of the powder bed and heat source–powder interaction behavior.

4. Discussion

4.1. Analysis of heat transfer characteristics of the powder bed

It is evident from the above experimental and simulation results that the existence of the powder layer and variations in its thickness change the PBF-EB fusion efficiency and molten pool geometry, which must be correlated with the heat transfer characteristics of the powder bed. Unlike the laser heat source, the electron beam penetrates the material almost without reflection. Consequently, the heat transfer characteristics during PBF-EB are determined primarily by the thermophysical properties of the powder bed. In particular, the effectively absorbed heat and the subsequent molten pool forming behavior are influenced by the emissivity and thermal conductivity of the powder bed [41].

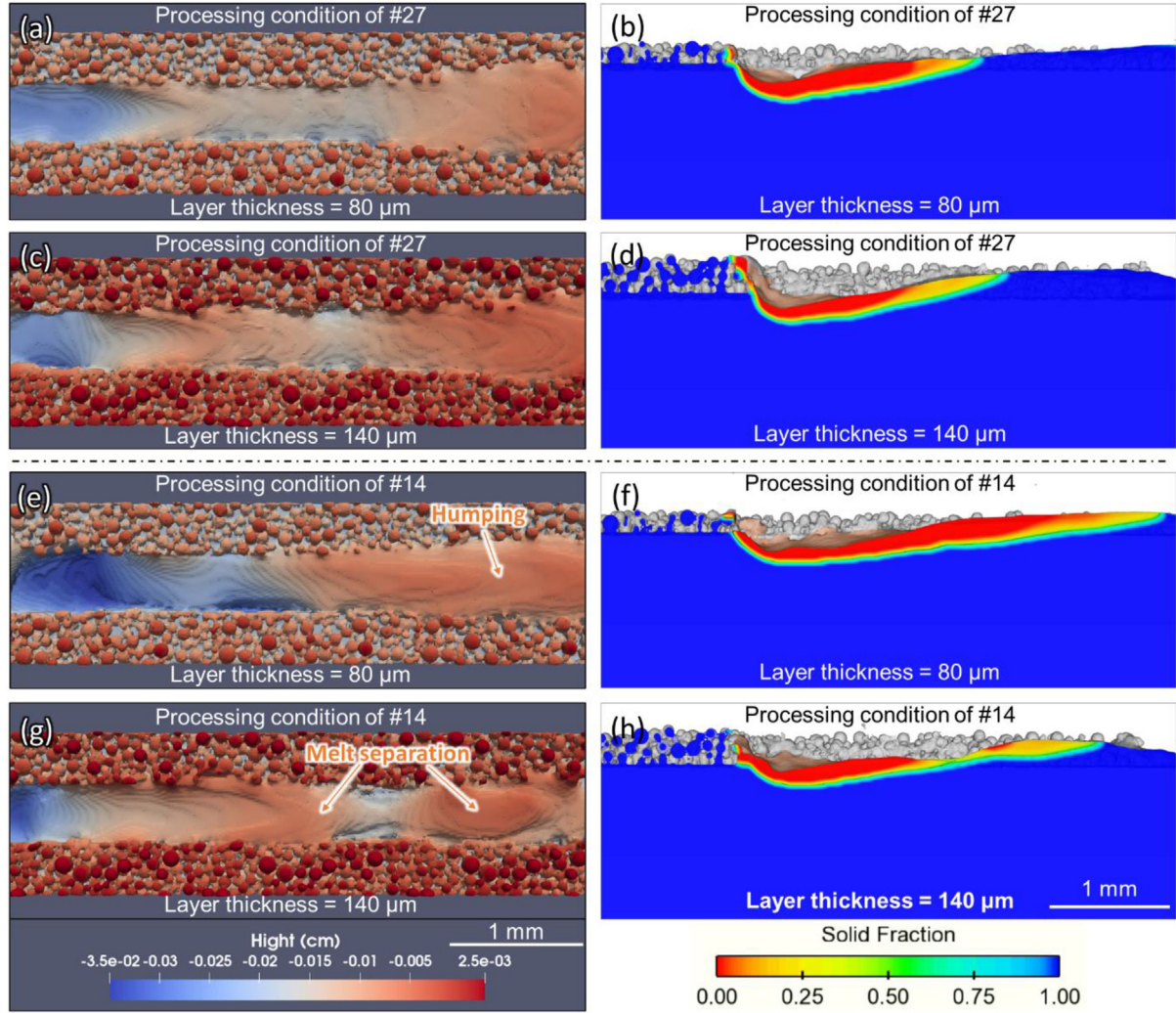


Fig. 8 – CtFD simulations of single-track fusion are implemented with the nominal layer thickness of (a) (b) (e) (f) 80 and (c) (d) (g) (h) 140 μm . (a) (c) (e) (g) Simulated melt-track profile after fusion and (b) (d) (f) (h) the molten pool geometry during the single-track melting simulation with the processing conditions of (a) (b) (c) (d) sample #27 ($P = 300\text{ W}$, $V = 186.94\text{ mm/s}$) and (e) (f) (g) (h) sample #14 ($P = 600\text{ W}$, $V = 412.36\text{ mm/s}$).

During the interaction between EB and powder bed, the energy loss (power, W) through heat radiation is proportional to the product of powder bed emissivity (ϵ_{bed}) and surface area of EB irradiated region (A) and accordingly, affects the absorbed heat [42]. Consequently, the higher the ϵ_{bed} and the larger the A , the less effective the heat absorption. A increases with the increased powder layer thickness; and then how the emissivity changes with layer thickness needs to be concerned. Thermal conductivity refers to the ability of a material to transfer or conduct heat. The powder bed with low thermal conductivity hinders the heat conveyed to the surrounding powder or substrate, restraining the molten pool progression. According to the literature [21], emissivity (ϵ_{bed}) and thermal conductivity (κ_{bed}) of a powder bed depend on the powder packing features. The ϵ_{bed} can be expressed as follows:

$$\epsilon_{\text{bed}} = F_{\text{pc}}\epsilon_{\text{pc}} + (1 - F_{\text{pc}})\epsilon_{\text{s}}, \quad (1)$$

$$\epsilon_{\text{pc}} = A_{\text{h}}\epsilon_{\text{h}} + (1 - A_{\text{h}})\epsilon_{\text{s}}, \quad (2)$$

$$A_{\text{h}} = \frac{0.908\varphi_{\text{pc}}^2}{1.908\varphi_{\text{pc}}^2 - 2\varphi_{\text{pc}} + 1}, \quad \epsilon_{\text{h}} = \frac{\epsilon_{\text{s}} \left[2 + 3.082 \left(\frac{1 - \varphi_{\text{pc}}}{\varphi_{\text{pc}}} \right)^2 \right]}{\epsilon_{\text{s}} \left[1 + 3.082 \left(\frac{1 - \varphi_{\text{pc}}}{\varphi_{\text{pc}}} \right)^2 \right] + 1}, \quad (3)$$

$$\varphi_{\text{pc}} = 1 - \frac{1 - \varphi}{F_{\text{pc}}}. \quad (4)$$

The κ_{bed} can be expressed as follows:

$$\kappa_{\text{bed}} = F_{\text{pc}} \left\{ \left(1 - \sqrt{1 - \varphi_{\text{pc}}} \right) \varphi_{\text{pc}} \kappa_{\text{r}} + \sqrt{1 - \varphi_{\text{pc}}} \left[(1 - \Lambda) \kappa_{\text{r}} + \phi \kappa_{\text{s}} \right] \right\} + (1 - F_{\text{pc}}) \kappa_{\text{s}}, \quad (5)$$

$$\kappa_{\text{r}} = \frac{4\epsilon_{\text{pc}}\sigma T_{\text{s}}^3 X_{\text{r}}}{1 - 0.132\epsilon_{\text{pc}}}, \quad (6)$$

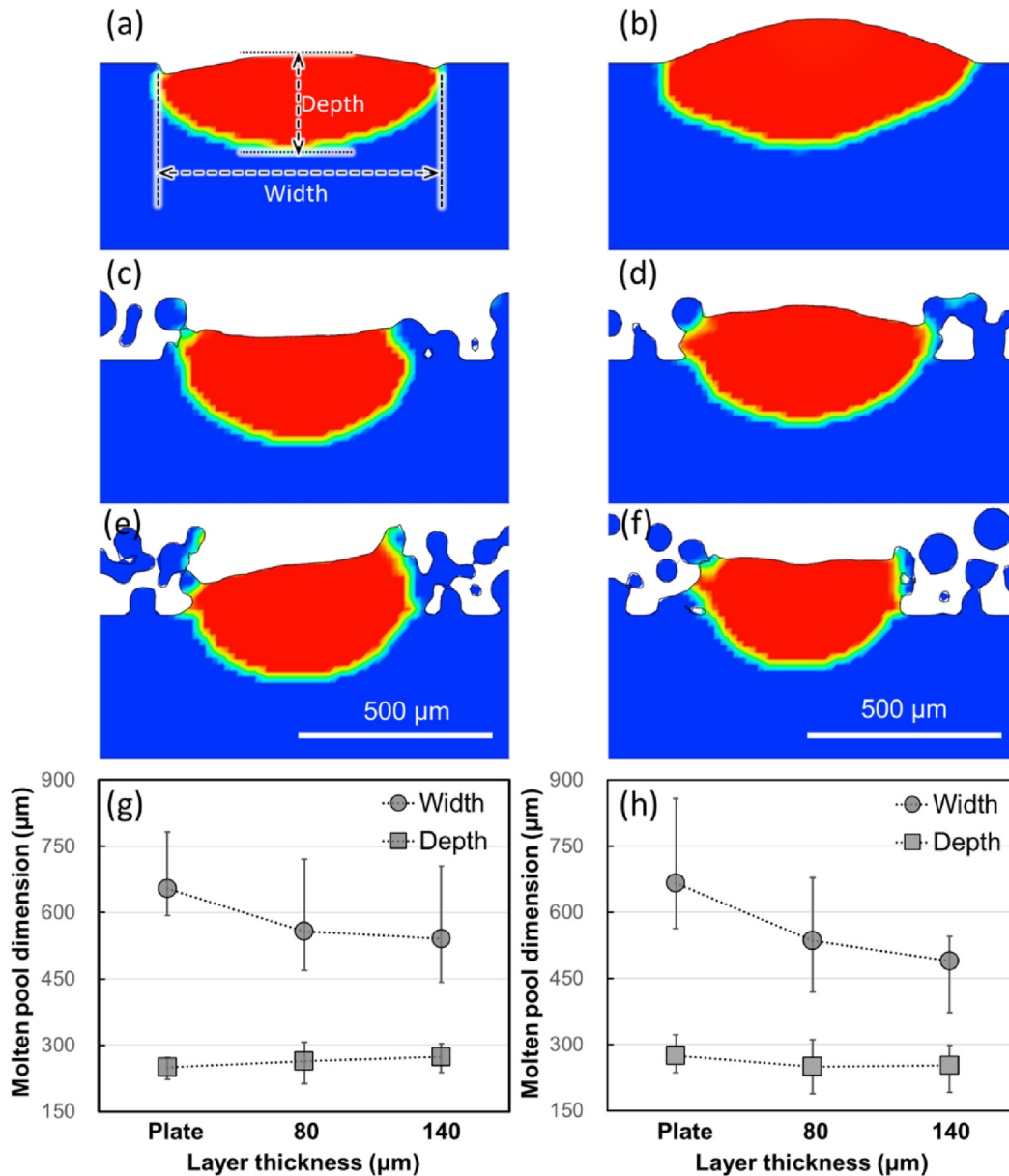


Fig. 9 – Cross sections and corresponding dimensional data of the melt tracks under the processing conditions of (a) (c) (e) (g) low (sample #27) and (b) (d) (f) (h) high power and scan speed (sample #14). (a) (b) Herein, the fusion simulation case on a bare plate without powder is complemented for reference. The powder layer thicknesses are (c) (d) 80 and (e) (f) 140 μm.

where Λ is the fractional contact area of solid-solid contact; X_r is the effective length for the radiation between the particles or the diameter of the particles. ϵ_{bed} and κ_{bed} are functions of the fractional packing porosity (φ), the area fraction of the powder coverage region on the projected plane (F_{pc}), temperature-dependent emissivity (ϵ_s) and thermal conductivity (κ_s) of the solid material. The values of Λ , X_r , φ and F_{pc} for different powder layer thicknesses can be derived from the DEM-simulated powder bed, as shown in Fig. 7. Temperature field data T_s under different processing conditions were obtained from the CtFD simulations. Fig. 10 shows the calculated ϵ_{bed} and κ_{bed} of the powder bed with different powder layer thicknesses under the

processing conditions of low power (sample #27) and high power and scan speed (sample #14).

With increased powder layer thickness, the emissivity and thermal conductivity show upward and downward trends, respectively. It is worth noting that thermal conductivity is not positively correlated with the increase in packing density with layer thickness, as the increase in the specific surface area of the powder layer hinders heat transfer between solid phases. The thick powder layer exhibits less effective heat absorption during the electron beam irradiation, and the heat conduction is limited; thus, the melt progression (especially along the width direction) is hindered. This explains why the powder layer and

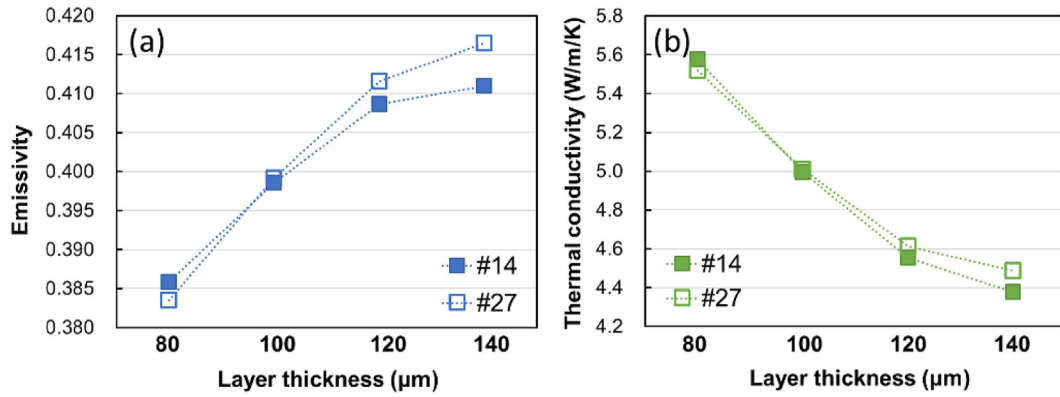


Fig. 10 – Calculated (a) emissivity and (b) thermal conductivity of powder bed with different powder layer thickness under the processing conditions of low (sample #27) and high power and scan speed (sample #14).

the increased layer thickness reduce the fusion efficiency (molten pool volume) and molten pool width, as discussed in Section 3.3. The reduced fusion efficiency, to some extent, restricts the height difference between the front and rear ends of the melt track caused by overheating (decreased S_a), whereas the reduction in the molten pool width enhances the Rayleigh–Plateau instability of the melt, resulting in local uplifts and conspicuous texture (increased S_{ar}).

4.2. Dependence of layer thickness-effect on processing conditions

The above experimental and simulation results indicate that the layer thickness has little effect on the heat and mass

transfer behavior when the power and scan speed are low. By contrast, higher power and scan speed strengthens the impact of the layer thickness on the heat-source–powder interaction process. Fig. 11 shows the evolution of the average temperature of the computational domain and molten pool volume during the single-track fusion simulation process.

The average temperature difference (Fig. 11(a) and (b)) can only be manifested under high power and scan-speed conditions. Similarly, the molten pool volume (Fig. 11(c) and (d)) demonstrates the above evolution trend—that is, under the conditions of high power and scan speed, the appearance of the powder layer and the increase in its thickness reduce the energy absorption. Consequently, the effect of the powder on the processing conditions is worth clarifying.

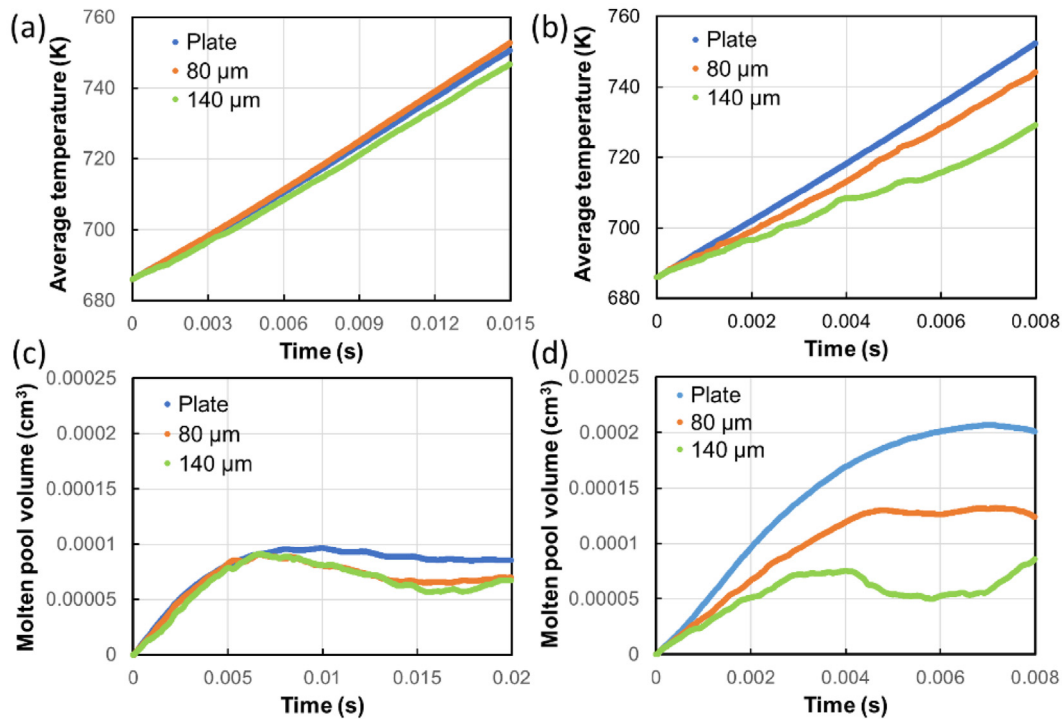


Fig. 11 – Under the processing conditions of (a) (c) low (sample #27) and (b) (d) high power and scan speed (sample #14), the evolution results of (a) (b) average temperature and (c) (d) molten pool volume in the corresponding computational domain during the single-track fusion simulation process.

As described in the previous section, compared with the bare plate, the existence of the powder layer causes the emissivity and thermal conductivity to differ from those of the solid material, varying with layer thickness. It is worth noting that when the powder particles melt, the reduction in heat absorption and transfer resistance caused by the porous powder bed is inactive. As the complete melting of the powder particles needs to take place over a certain time span, the melted and incomplete melted powder coexist in the area irradiated by the moving electron beam heat source. The larger the proportion of incomplete melted powder in the irradiation area, the greater the effect of the powder layer and its thickness variation on energy absorption and heat transfer.

Fig. 12 shows the simulated visualization results of the relationship between the electron beam irradiation area on the powder bed surface and the melt formed during the fusion process.

Compared with the bare plate, the front end of the melt on the powder bed lags the front edge of the heat source, the lagging extent being greater with an increase in the layer thickness. This is exactly the embodiment of the blocking effect on the heat absorption and transfer caused by the powder layer and its increased thickness. More importantly, comparing the results under the two processing conditions, it is evident that the lagging extent of the melt relative to the heat source is more notable at high power and scan speed

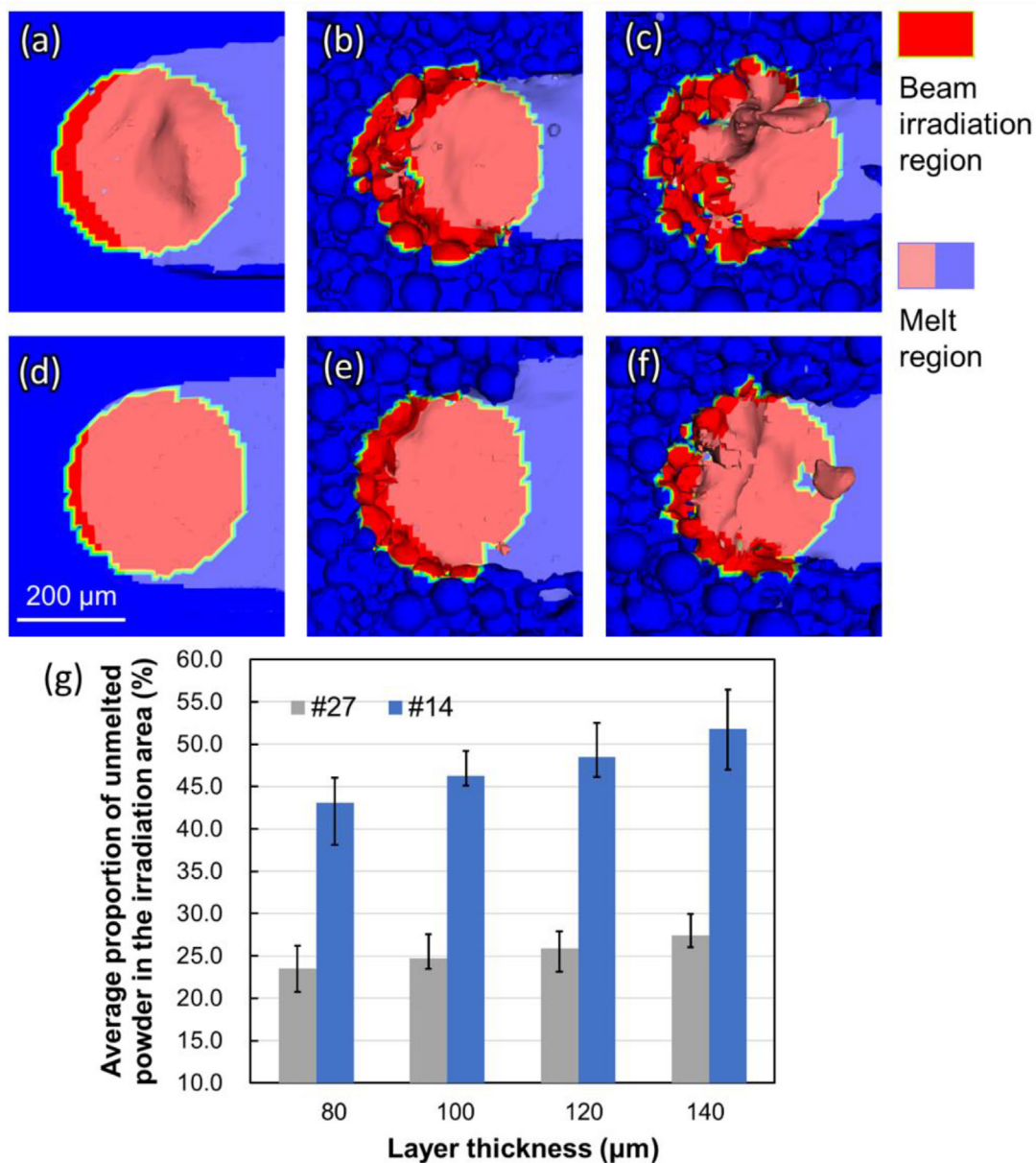


Fig. 12 – Simulated visualization results of the relationship between the electron beam irradiation area and the formed melt during the fusion process on (a) (d) bare plate, (b) (e) 80 and (c) (f) 140-μm powder layer and under the processing conditions of (a) (b) (c) high (sample #14) and (d) (e) (f) low power and scan speed (sample #27). (g) The average proportion of incomplete melted powder in the irradiation area with the different powder layer thicknesses.

(sample #14) than at low power and scan speed (sample #27). This phenomenon is caused primarily by the difference in scan speed—that is, the faster the scan speed, the greater the distance difference between the front edge of the heat source and the front end of the melt obtained within the time span from heating the powder to complete melting. Consequently, at a relatively high scan speed, the proportion of incomplete melted powder in the area irradiated by the heat source is larger, and the influence of the powder layer on heat and mass transfer is more substantial.

Fig. 12(g) shows the average proportion of incomplete melted powder in the irradiation area with different powder layer thicknesses. With an increase in the layer thickness, the emissivity and thermal conductivity of the powder layer increase and decrease, respectively, extending the time span from powder heating to complete melting. Consequently, at a certain scan speed, the distance difference between the heat source and the melt increases—that is, the proportion of the incomplete melted powder area increases. The proportion of the incomplete melted powder area increases, especially at high scan speeds, and the powder effect can be brought into full play; that is, the above evolution trend is greater with increasing layer thickness, thereby leading to substantial changes in melt behavior.

The hindering effect on heat absorption and transfer caused by the powder layer and its increased thickness depends primarily on the beam scan speed. The influence of the layer thickness variation on the melt behavior and the corresponding fusion surface morphology is embodied mainly at high scan speeds.

5. Conclusions

Four batches of cylindrical specimens with increasing layer thicknesses from 80 to 140 μm were prepared by PBF-EB within the same range of processing parameters. Processing windows for different powder layer thicknesses were derived. The evolution trends of the upper surface roughness with layer thickness were analyzed. Combined with thermophysical-property analysis of the powder bed and numerical simulation of fusion, the influence mechanism of the layer thickness on the melt behavior and resultant surface quality was revealed, and the dependence of the layer thickness-effect on the processing conditions was clarified. The main conclusions to be drawn were as follows:

- 1) Within the processing regime of the present study, a relatively high powder layer thickness expands the processing window. The mean values of S_a (indicator for height fluctuation/difference) and S_{dr} (indicator for surface texture/stripes) decrease and increase, respectively, with increasing layer thickness. A high layer thickness helps restrain the fluctuation and reduce the height difference within the overall area of the sample upper surface sample. Nevertheless, the increase in S_{dr} indicated that a high layer thickness contributed to the formation of a rough surface texture.
- 2) The emissivity and thermal conductivity exhibited upward and downward trends with increased powder layer

thickness, respectively. The increased powder layer thickness reduced the fusion efficiency (molten pool volume) and molten pool width, restricting the height difference within the overall sample surface caused by overheating (decreased S_a); whereas the reduction in the molten pool width enhanced the Rayleigh–Plateau instability of the melt, resulting in local uplifts and conspicuous texture (increased S_{dr}).

- 3) At a high scan speed, the proportion of incomplete melted powder in the area irradiated by the electron beam heat source increased. Consequently, the hindering effect on heat absorption and transfer caused by the powder layer and its increased thickness was fully manifested. That is, the evolution trend of melt behavior and surface morphology resulting from increased layer thickness is remarkable at high scan speeds.

Credit author statement

Yufan Zhao: Writing - Original Draft, Conceptualization, Investigation, Visualization.

Kenta Aoyagi: Writing - Review & Editing, Resources, Methodology.

Kenta Yamanaka: Supervision.

Akihiko Chiba: Writing - Review & Editing, Supervision, Funding acquisition.

Declaration of competing interest

The authors declare that they have no known competing financial interests or personal relationships that could have appeared to influence the work reported in this paper.

Acknowledgments

Thanks are due to JAMPT Corporation for providing the PREP powders and PBF-EB building trials. This work was supported by JSPS KAKENHI [Grant Numbers 18H03834 and 18H05455]. It was also supported by the “Materials Integration for Revolutionary Design System of Structural Materials” of the Cross-Ministerial Strategic Innovation Promotion Program (SIP) at Japan Science and Technology (JST). This study was based on the results of the “Creation of Life Innovation Materials for Interdisciplinary and International Researcher Development” project. This paper was based on the results obtained from a project commissioned by the New Energy and Industrial Technology Development Organization (NEDO) [Grant Numbers JPNP14014 and JPNP19007]. This work was also supported by the Technology Research Association for Future Additive Manufacturing (TRAFAM); the Research Fund of the State Key Laboratory of Solidification Processing, NPU, China [Grant Number 2023-TS-10]; the Guangdong Basic and Applied Basic Research Foundation [Grant Number 2022A1515110242] and the Natural Science Basis Research Plan in Shaanxi Province of China [Grant Number 2022JQ-479]. We want to thank Editage (www.editage.com) for the English language editing.

REFERENCES

- [1] Tan XP, Tan YJ, Chow CSL, Tor SB, Yeong WY. Metallic powder-bed based 3D printing of cellular scaffolds for orthopaedic implants: a state-of-the-art review on manufacturing, topological design, mechanical properties and biocompatibility. *Mater Sci Eng, C* 2017;76:1328–43. <https://doi.org/10.1016/j.msec.2017.02.094>.
- [2] Galati M, Snis A, Iuliano L. Powder bed properties modelling and 3D thermo-mechanical simulation of the additive manufacturing Electron Beam Melting process. *Addit Manuf* 2019;30:100897. <https://doi.org/10.1016/j.addma.2019.100897>.
- [3] Ruan G, Liu C, Qu H, Guo C, Li G, Li X, et al. A comparative study on laser powder bed fusion of IN718 powders produced by gas atomization and plasma rotating electrode process. *Mater Sci Eng, A* 2022;850:143589. <https://doi.org/10.1016/j.msea.2022.143589>.
- [4] Shui X, Yamanaka K, Mori M, Nagata Y, Kurita K, Chiba A. Effects of post-processing on cyclic fatigue response of a titanium alloy additively manufactured by electron beam melting. *Mater Sci Eng, A* 2017;680:239–48. <https://doi.org/10.1016/j.msea.2016.10.059>.
- [5] Lee Y, Gurnon AK, Bodner D, Simunovic S. Effect of particle spreading dynamics on powder bed quality in metal additive manufacturing. *Integr Mater Manuf Innov* 2020;9:410–22. <https://doi.org/10.1007/s40192-020-00193-1>.
- [6] Leung CLA, Marussi S, Towrie M, Atwood RC, Withers PJ, Lee PD. The effect of powder oxidation on defect formation in laser additive manufacturing. *Acta Mater* 2019;166:294–305. <https://doi.org/10.1016/j.actamat.2018.12.027>.
- [7] Galati M, Snis A, Iuliano L. Experimental validation of a numerical thermal model of the EBM process for Ti6Al4V. *Comput Math Appl* 2019;78:2417–27. <https://doi.org/10.1016/j.camwa.2018.07.020>.
- [8] Körner C. Additive manufacturing of metallic components by selective electron beam melting - a review. *Int Mater Rev* 2016;61:361–77. <https://doi.org/10.1080/09506608.2016.1176289>.
- [9] Li H, Yu Y, Li Y, Lin F. Effects of the higher accelerating voltage on electron beam powder-bed based additive manufacturing of Ti6Al4V alloy. *Addit Manuf* 2022;50:102579. <https://doi.org/10.1016/j.addma.2021.102579>.
- [10] Mussatto A, Groarke R, O'Neill A, Obeidi MA, Delaure Y, Brabazon D. Influences of powder morphology and spreading parameters on the powder bed topography uniformity in powder bed fusion metal additive manufacturing. *Addit Manuf* 2021;38:101807. <https://doi.org/10.1016/j.addma.2020.101807>.
- [11] Penny RW, Praegla PM, Ochsenius M, Oropeza D, Weissbach R, Meier C, et al. Spatial mapping of powder layer density for metal additive manufacturing via transmission X-ray imaging. *Addit Manuf* 2021;46:102197. <https://doi.org/10.1016/j.addma.2021.102197>.
- [12] Nath SD, Gupta G, Kearns M, Gulsoy O, Atre SV. Effects of layer thickness in laser-powder bed fusion of 420 stainless steel. *Rapid Prototyp J* 2020;26:1197–208. <https://doi.org/10.1108/RPJ-10-2019-0279>.
- [13] Shi X, Ma S, Liu C, Chen C, Wu Q, Chen X, et al. Performance of high layer thickness in selective laser melting of Ti6Al4V. *Materials* 2016;9:975. <https://doi.org/10.3390/ma9120975>.
- [14] Leicht A, Fischer M, Klement U, Nyborg L, Hryha E. Increasing the productivity of laser powder bed fusion for stainless steel 316L through increased layer thickness. *J Mater Eng Perform* 2021;30:575–84. <https://doi.org/10.1007/s11665-020-05334-3>.
- [15] Badrossamay M, Rezaei A, Foroozmehr E, Maleki A, Foroozmehr A. Effects of increasing powder layer thickness on the microstructure, mechanical properties, and failure mechanism of IN718 superalloy fabricated by laser powder bed fusion. *Int J Adv Manuf Technol* 2022;118:1703–17. <https://doi.org/10.1007/s00170-021-07719-7>.
- [16] Ye J, Khairallah SA, Rubenchik AM, Crumb MF, Guss G, Belak J, et al. Energy coupling mechanisms and scaling behavior associated with laser powder bed fusion additive manufacturing. *Adv Eng Mater* 2019;21:1900185. <https://doi.org/10.1002/adem.201900185>.
- [17] de Terris T, Andreau O, Peyre P, Adamski F, Koutiri I, Gorny C, et al. Optimization and comparison of porosity rate measurement methods of Selective Laser Melted metallic parts. *Addit Manuf* 2019;28:802–13. <https://doi.org/10.1016/j.addma.2019.05.035>.
- [18] Meier C, Penny RW, Zou Y, Gibbs JS, Hart AJ. Thermophysical phenomena in metal additive manufacturing by selective laser melting: fundamentals, modeling, simulation, and experimentation. *Annu Rev Heat Transf* 2018;20:241–316. <https://doi.org/10.1615/annualrevheattransfer.2018019042>.
- [19] Carriere PR, Yue S. Energy absorption during pulsed electron beam spot melting of 304 stainless steel: monte-Carlo simulations and in-situ temperature measurements. *Vacuum* 2017;142:114–22. <https://doi.org/10.1016/j.vacuum.2017.04.039>.
- [20] Yang Y, Gu D, Dai D, Ma C. Laser energy absorption behavior of powder particles using ray tracing method during selective laser melting additive manufacturing of aluminum alloy. *Mater Des* 2018;143:12–9. <https://doi.org/10.1016/j.matdes.2018.01.043>.
- [21] Zhao Y, Koizumi Y, Aoyagi K, Yamanaka K, Chiba A. Thermal properties of powder beds in energy absorption and heat transfer during additive manufacturing with electron beam. *Powder Technol* 2021;381:44–54. <https://doi.org/10.1016/j.powtec.2020.11.082>.
- [22] Li H, Liang X, Li Y, Lin F. Performance of high-layer-thickness Ti6Al4V fabricated by electron beam powder bed fusion under different accelerating voltage values. *Materials* 2022;15:1878. <https://doi.org/10.3390/ma15051878>.
- [23] Narra SP, Cunningham R, Beuth J, Rollett AD. Location specific solidification microstructure control in electron beam melting of Ti-6Al-4V. *Addit Manuf* 2018;19:160–6. <https://doi.org/10.1016/j.addma.2017.10.003>.
- [24] Charles A, Elkaseer A, Thijs L, Hagenmeyer V, Scholz S. Effect of process parameters on the generated surface roughness of down-facing surfaces in selective laser melting. *Appl Sci* 2019;9:1256. <https://doi.org/10.3390/app9061256>.
- [25] Nagalingam AP, Yeo SH. Surface finishing of additively manufactured Inconel 625 complex internal channels: a case study using a multi-jet hydrodynamic approach. *Addit Manuf* 2020;36:101428. <https://doi.org/10.1016/j.addma.2020.101428>.
- [26] Šmilauer Václav, Catalano Emanuele, Bruno Chareyre, Dorofeenko Sergei, Jerome Duriez, Nolan Dyck, et al. Yade documentation. second ed. The Yade Project; 2015. <https://doi.org/10.5281/zenodo.34073>.
- [27] Šmilauer V, Chareyre B. Yade DEM formulation. *Yade Doc* 2010;2011:38.
- [28] Peng B. Discrete element method (DEM) contact models applied to pavement simulation. Virginia Polytechnic Institute and State University; 2014.
- [29] Chen Q, Zhao Y, Strayer S, Zhao Y, Aoyagi K, Koizumi Y, et al. Elucidating the effect of preheating temperature on melt pool morphology variation in Inconel 718 laser powder bed fusion via simulation and experiment. *Addit Manuf* 2021;37:101642. <https://doi.org/10.1016/j.addma.2020.101642>.

- [30] FlowScience I. FLOW-3D® version 11.2 [computer software]. 2017.
- [31] Shen N, Chou K. Thermal modeling of electron beam additive manufacturing process - powder sintering effects. ASME 2012 Int Manuf Sci Eng Conf Collocated with 40th North Am Manuf Res Conf Particip with Int Conf, MSEC 2012;2012:287. <https://doi.org/10.1115/MSEC2012-7253>. 95.
- [32] Zhao Y, Aoyagi K, Yamanaka K, Chiba A. Role of operating and environmental conditions in determining molten pool dynamics during electron beam melting and selective laser melting. Addit Manuf 2020;36:101559. <https://doi.org/10.1016/j.addma.2020.101559>.
- [33] Messler RW. Principles of welding. Weinheim, Germany: Wiley-VCH Verlag GmbH; 1999. <https://doi.org/10.1002/9783527617487>.
- [34] Zhao Y, Koizumi Y, Aoyagi K, Wei D, Yamanaka K, Chiba A. Molten pool behavior and effect of fluid flow on solidification conditions in selective electron beam melting (SEBM) of a biomedical Co-Cr-Mo alloy. Addit Manuf 2019;26:202–14. <https://doi.org/10.1016/j.addma.2018.12.002>.
- [35] Zhao Y, Bian H, Wang H, Kenta A, Kenta Y, Chiba A. Non-equilibrium solidification behavior associated with powder characteristics during electron beam additive manufacturing. Mater Des 2022;221:110915. <https://doi.org/10.1016/j.matdes.2022.110915>.
- [36] Meier C, Weissbach R, Weinberg J, Wall WA, Hart AJ. Critical influences of particle size and adhesion on the powder layer uniformity in metal additive manufacturing. J Mater Process Technol 2019;266:484–501. <https://doi.org/10.1016/j.jmatprotec.2018.10.037>.
- [37] Xiang Z, Zhang M, Yan R, Yin Q, Zhang K. Powder-spreading dynamics and packing quality improvement for laser powder bed fusion additive manufacturing. Powder Technol 2021;389:278–91. <https://doi.org/10.1016/j.powtec.2021.05.036>.
- [38] Wu C, Zafar MQ, Zhao H, Wang Y, Schöler C, Heinigk C, et al. Multi-physics modeling of side roughness generation mechanisms in powder bed fusion. Addit Manuf 2021;47:102274. <https://doi.org/10.1016/j.addma.2021.102274>.
- [39] Guo Q, Zhao C, Qu M, Xiong L, Hojjatzadeh SMH, Escano LI, et al. In-situ full-field mapping of melt flow dynamics in laser metal additive manufacturing. Addit Manuf 2020;31:100939. <https://doi.org/10.1016/j.addma.2019.100939>.
- [40] Mishra AK, Kumar A. Modelling of SLM additive manufacturing for magnesium alloy. 123–40, https://doi.org/10.1007/978-981-10-8767-7_5; 2018.
- [41] Sumin Sih S, Barlow JW. The prediction of the emissivity and thermal conductivity of powder beds. Part Sci Technol 2004;22:291–304. <https://doi.org/10.1080/02726350490501682a>.
- [42] Zhao Y, Aoyagi K, Daino Y, Yamanaka K, Chiba A. Significance of powder feedstock characteristics in defect suppression of additively manufactured Inconel 718. Addit Manuf 2020;34:101277. <https://doi.org/10.1016/j.addma.2020.101277>.